International Journal of Biological Macromolecules 328 (2025) 147401

Contents lists available at ScienceDirect

International Journal of Biological Macromolecules

journal homepage: www.elsevier.com/locate/ijbiomac

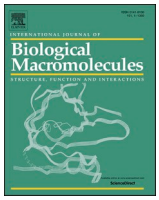

# Hydrostatic pressure response of α-keratin investigated with Raman spectroscopy

A.M. Paschou [a], D. Christofilos [b], J. Arvanitidis [a], E. Pavlidou [a], I. Zizak [c], M. Katsikini [a,*]

[a] School of Physics, Aristotle University of Thessaloniki, 54124, Thessaloniki, Greece
[b] School of Chemical Engineering & Laboratory of Physics, Faculty of Engineering, Aristotle University of Thessaloniki, 54124, Thessaloniki, Greece
[c] Helmholtz Zentrum Berlin für Materialien und Energie, Albert Einstein Str. 15, 12489, Berlin, Germany

ARTICLE INFO

*Keywords:*
Keratin
Raman spectroscopy
High pressure
Amide-I
Small Angle X-ray Scattering

ABSTRACT

Keratins represent an important class of sulfur-rich structural proteins. In this study, the pressure response of α-keratin, extracted from sheep wool, was investigated using Raman spectroscopy up to 4 GPa. A non-polar liquid (a Fluorinert™ FC70/77 mixture) served as the Pressure Transmitting Medium (PTM) in a Diamond Anvil Cell (DAC). Scanning Electron Microscopy (SEM) and Small-Angle X-ray Scattering (SAXS) were used for the morphological and structural characterization of the sample. Three Raman bands were monitored during compression and decompression: C—H deformation, amide-I (dominated by the C═O stretching vibration of the peptide bond) and C—H stretching vibrations centered at approximately 1450, 1670 and 2940 $cm^{-1}$, respectively. The deformation modes of the C—H bonds exhibited a weak positive pressure dependence (~1.7 $cm^{-1}$/GPa), whereas the corresponding stretching modes showed a much stronger dependence (6–9 $cm^{-1}$/GPa). A positive slope (~2.2 $cm^{-1}$/GPa) was also observed for the amide-I band, consistent with C═O strengthening in the peptide bonds under compression. This behavior contrasts with that of collagen, which exhibits a negative pressure slope for the same vibrational mode. The opposite responses are discussed in relation to the different structural roles of hydrogen bonding in these two fibrous proteins. Overall, the response of keratin to high hydrostatic pressure is reversible.

## 1. Introduction

Keratins comprise an important class of structural proteins that have a wide range of medical, cosmetic and industrial applications owing to their biocompatibility and biodegradability [1]. They are found in epithelial cells, hair, skin, nails, feathers, and other biological materials and play a crucial role in providing mechanical resilience, protection, and thermal insulation [2,3]. In addition, keratins form lightweight structures and hydrophobic surfaces, and in some cases contribute to structural coloration and even reversible adhesion [4]. Due to their hierarchical structure, keratins are characterized by remarkable strength, while maintaining a high degree of flexibility. Although their properties at ambient conditions have been extensively studied [5,6], their behavior under high-pressure remains an active area of research. The application of high-pressure can induce changes in molecular structure and affect intermolecular interactions, potentially altering the mechanical, chemical, and biological properties of keratin [7]. The study of these pressure-induced transformations provides valuable insights, not only into the fundamental behavior of keratin as a biomaterial, but also into its implications across various fields, from materials science to medicine, including applications in tumor diagnostics [8] and immunohistochemistry [9]. Gene mutations in human keratins have also been linked to several diseases [10]. Other biomedical applications of keratin can be found in bone tissue engineering [11,12], wound healing [13,14], and ocular [15], nerve [16,17], and skin [18] regeneration as well as controlled drug delivery [19]. Keratin-based products can be processed into diverse forms such as films, hydrogels, scaffolds and composites [20]. Finally, the unique physicochemical properties of keratin-based biomaterials enable their use in energy, agriculture, cosmetics, the leather and textile industries, and in emerging areas such as natural polymer flocculants, absorbents, biolubricants and bioelectronics [21].

The mechanical properties of a single-chain biological molecule are generally determined by the type and strength of its bonds, primarily covalent and hydrogen (H-) bonds, and to a lesser extent by its interactions with more distant neighbors. However, many fibrous proteins

* Corresponding author.
*E-mail address:* katsiki@auth.gr (M. Katsikini).

https://doi.org/10.1016/j.ijbiomac.2025.147401
Received 6 July 2025; Received in revised form 17 August 2025; Accepted 3 September 2025
Available online 4 September 2025

owe their unique mechanical behavior to their hierarchical structure. In the case of α-keratin, the hierarchical organization, from the formation of individual chains to the assembly of intermediate filaments (IFs) [2], is illustrated in Fig. 1(a). Peptide bonds between adjacent amino acid (AA) residues form the polypeptide chain, where H-bonding plays a central role in determining the secondary structure. α-Keratins consist predominantly of α-helical segments separated by short non-helical linker regions. At the ends of the rod domain, globular C- and N-terminal domains are present, both rich in sulfur-containing AAs. The AA sequences in the head domain and the linkers of the rod domain tend to favor a β-turn structure [22,23]. Approximately 38–45 % of the keratin molecule structure adopts the α-helical conformation [24]. The coiled-coil segments are formed by two different right-handed α-helices, with 0.51 nm vertical distance between consecutive turns [25], which twist around each other to form a right-handed heterogeneous dimer. In nearly all IF proteins, a characteristic heptad repeat sequence $(a\text{-}b\text{-}c\text{-}d\text{-}e\text{-}f\text{-}g)_n$ is present. It is schematically shown in Fig. 1(b). Positions a and d are predominantly occupied (~75 %) by nonpolar (hydrophobic) residues such as Leucine (Leu), Valine (Val) and Isoleucine (Ile), while positions e and g are commonly filled with charged residues, such as Glutamic Acid (Glu), Aspartic Acid (Asp), Lysine (Lys) and Arginine (Arg). This arrangement enables the "knob and hole" packing of two α-helices into a stable coiled-coil dimer [26,27]. Two dimers entwine in an antiparallel arrangement to form a tetramer (protofilament) [28]. The hydrophobic interactions between dimers, which contribute to the stability of type I/II keratin tetramers, have been described by Bernot et al. [29]. Two protofilaments combine to form a protofibril, and four protofibrils assemble to create the final keratin IF. Disulfide bridges are formed both within and between IFs, further contributing to structural integrity [30]. Keratin IFs and low-sulfur Keratin Associated Proteins (KAPs) give rise to keratin microfibrils. At a higher structural level, these microfibrils, embedded in an amorphous matrix composed of high-S and high-Tyrosine (high-Tyr) KAPs, are arranged in a hexagonal close packed 2D lattice to form macrofibrils [31].

High-pressure Raman spectroscopy is a powerful, non-destructive technique for investigating the structural and vibrational properties of biological macromolecules, as well as their conformational changes under extreme conditions. It provides valuable insights into molecular stability, folding mechanisms, and interactions with various environments. Raman spectroscopy is highly sensitive to subtle changes in molecular vibrations induced by external factors, such as hydrostatic pressure, temperature, and modification in the bonding environment. It has been extensively employed to study conformational changes in hair keratin [32] as well as to examine the effect of chemical treatments [33,34], thermal exposure [35], and mechanical stress [36] on keratin structure. Moreover, Raman spectroscopy has been proved particularly effective in probing the high-pressure response of AAs [37–39] and other structural proteins [40].

This work examines the mechanical response of keratin under high-pressure conditions, with the aim of deepening our understanding of its behavior at the molecular level and particularly the extent of bond hardening, the behavior of hydrogen bonding during compression, and the reversibility upon decompression. To our knowledge, this is the first study on the investigation of the effect of hydrostatic pressure on this structural protein. The findings provide new insights into the structural adaptability and mechanical robustness of keratin at the molecular level, knowledge that is relevant to biomaterials science, particularly for the design of pressure-resistant keratin-based films, coatings, or composites, as well as to the broader understanding of protein dynamics under high-pressure. Complementary techniques, including Scanning Electron Microscopy (SEM) and Small Angle X-ray Scattering (SAXS), were employed to provide additional information on the morphology of the keratin powder grains and the packing of keratin IFs.

## 2. Materials and methods

The sample under study was α-keratin in powder form, extracted from sheep wool (CAS No. 69430-36-0, TCI). A kit with amino acids in powder form, purchased from AccuStandard, was used for the acquisition of reference Raman spectra. SEM images were acquired using a Jeol Field Emission (FESEM) 7610 FPLUS microscope, equipped with an OXFORD Aztec Energy Dispersive Spectrometry (EDS) microanalyzer.

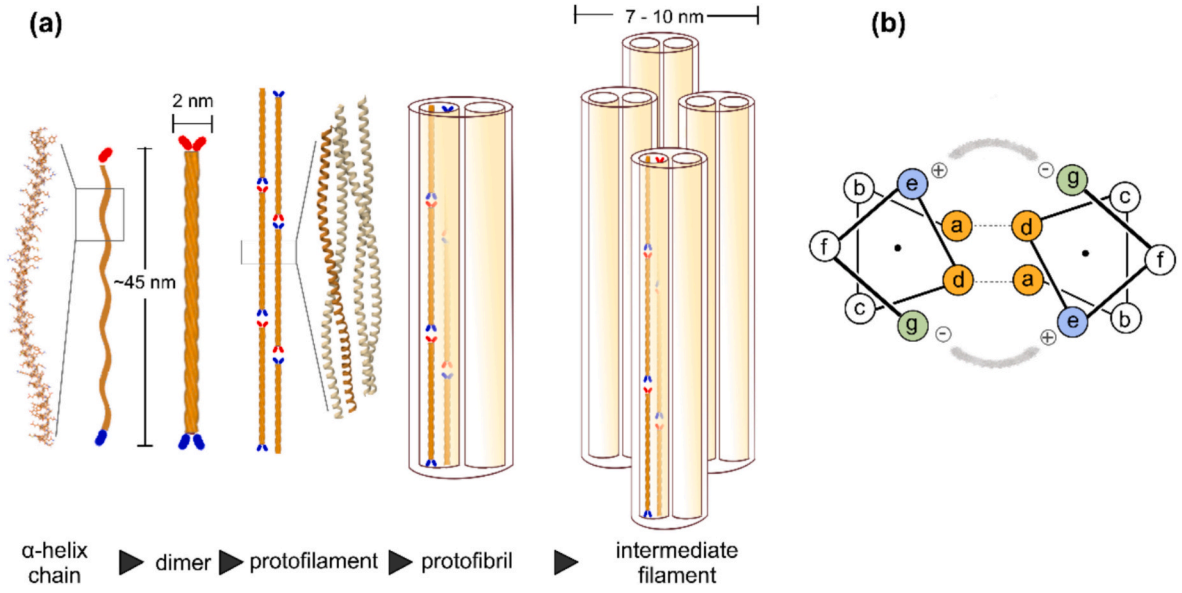


**Fig. 1.** (a) Structural hierarchy of α-keratin from the polypeptide chain to the formation of the intermediate filament; ball-and-stick model of the polypeptide chain in an α-helix conformation, with a vertical distance of 0.51 nm between successive turns of the helix. Two parallel α-helices twist around each other to form a coiled-coil dimer. Two such dimers associate in an antiparallel orientation to form a protofilament. Protofibrils consist of two protofilaments and four protofibrils assemble into a keratin intermediate filament. (b) Schematic representation of the cross-section of a two-stranded α-helical coiled-coil illustrating the heptad repeat (a–g) of AA residues, characteristic of the keratin coiled-coil structure. Positions "a" and "d" are typically occupied by hydrophobic residues, which align to the core of the heterodimer formed by the two α-helices. Positions "e" and "g" are commonly occupied by charged residues that contribute to electrostatic interactions stabilizing the structure. Part b is reproduced from Ref. 27.

Measurements were performed in low-vacuum mode, with operating conditions of 10 kV accelerating voltage, 15 nA probe current and a working distance of 10 mm. Two-dimensional (2D) SAXS patterns were recorded from sheep wool and the keratin powder at the mySpot beamline of the BESSY-II storage ring (Helmholtz Zentrum Berlin). The patterns were recorded using a beam with $\lambda = 1.127$ Å and a Dectris Eiger X 9M detector, whereas silver behenate was used to calibrate the sample-to-detector distance. A 30 μm pinhole was used for beam collimation, along with a 50 μm beamstop. In the case of the wool sample, a single fiber, mounted on a frame, was positioned nearly vertically and perpendicular to the X-ray beam. A SAXS pattern from the empty frame was recorded and used for background subtraction. For the keratin sample, the powder was placed between two thin cover slips, and the SAXS pattern of the empty cover slips was used for background subtraction. Integrated intensity curves were obtained using the DPDAK software [41].

Raman measurements were carried out using a LabRAM HR (HORIBA) spectrometer equipped with a microscope, using a 50× long working distance objective lens. The beam from a solid-state laser ($\lambda =$ 514.2 nm) was focused on the sample with a power of ~2 mW, measured before the microscope objective. Potential spectral shifts induced by the spectrometer were corrected using the emission lines of a Neon lamp. For the high-pressure measurements, a Mao-Bell type Diamond Anvil Cell (DAC) was used. Pressures up to approximately 4 GPa, were applied mechanically by tightening a screw, which brought the two diamond anvils closer, reducing the volume in the sample chamber. The latter consisted of a ~ 150 μm diameter hole drilled in a stainless-steel gasket, which contained the Pressure Transmitting Medium (PTM), the sample, and a small ruby chip for pressure calibration *via* its $R_1$ fluorescence line [42]. A non-polar fluorocarbon liquid mixture (1:1 Fluorinert FC70/FC77) was used as PTM. Raman spectra were recorded from several grains of the keratin sample at ambient conditions as well as from several spots on the tiny keratin sample placed in the DAC to verify the sample homogeneity. After background subtraction, Voigt functions were used to fit the keratin Raman peaks.

## 3. Results and discussion

### 3.1. Morphological and structural characterization

SEM was applied to obtain detailed information on the morphology of the keratin powder. Secondary electron SEM images, which are particularly sensitive to surface topography, were recorded from various sample spots and are shown in Fig. 2. As evident from the images, the powder grains were generally smaller than 10 μm and exhibited a layered structure.

Further structural information was obtained through SAXS analysis. Fig. 3(a) compares the 2D SAXS patterns from a sheep wool fiber and the keratin powder. In the case of wool, faint scattering arcs are observed in the equatorial direction. In contrast, the 2D scattering pattern of the keratin powder is isotropic, with no discernible arcs of rings, suggesting that the extraction process disrupted the packing of IFs within the macrofibrils [43]. The integrated scattering intensity curves (equatorially integrated for the wool fiber and pie integrated for keratin) are shown in Fig. 3(b). For the wool fiber, broad intensity maxima are evident at q ~ 0.7 and 1.2 $nm^{-1}$, corresponding to the lateral packing of the IFs. Azimuthally integrated intensity profiles for both samples are provided in the Supplementary Material (S1). To extract information on the size and the packing distance of the IFs, the I-q curve of keratin was simulated using the model proposed by Briki et al. [44]. According to this model, keratin IFs are embedded in an interfilamentous matrix and arranged in a distorted (paracrystal) hexagonal 2D lattice, with a lattice constant of approximately 10 nm [45]. In this framework, the electron density $\rho(\vec{r})$ is modeled as a periodic arrangement of identical "unit cells" positioned on the sites defined by a hexagonal lattice of constant a.

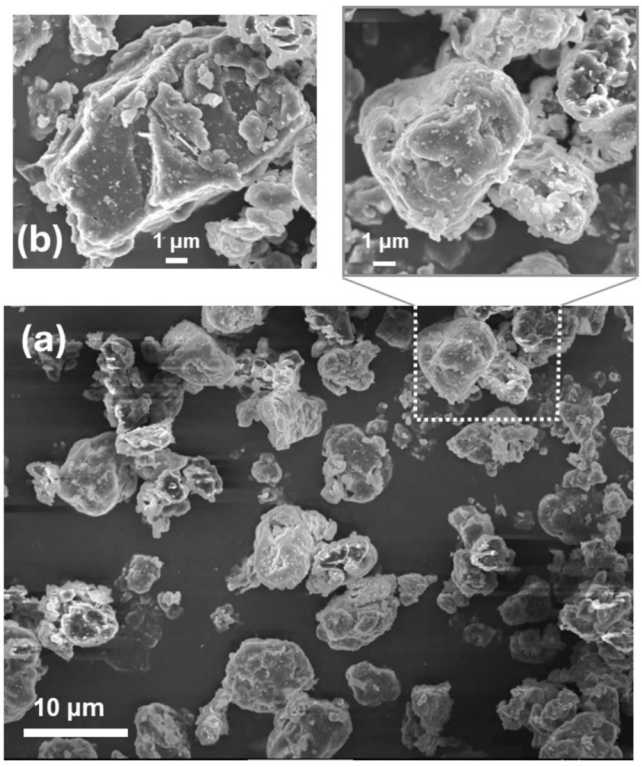


**Fig. 2.** Secondary Electron SEM images of α-keratin extracted from wool. (a) Powder grains smaller than 10 μm are observed, exhibiting a layered structure, which is clearly visible in (b) and the magnified region of (a).

The I-q curve was simulated using the following equation:

$$I(q) = I_{BG} + Z(q)\left(|F_{if}(q)|^2 + |F_{mat}(q)|^2\right) \quad (1)$$

where $I_{BG}$ is the background intensity, Z(q) is the interference function (structure factor) that accounts for the arrangement of the IFs within the macrofibrils, $F_{if}$ is the form factor of the IFs and $F_{mat}$ represents the contribution from the interfilamentous matrix surrounding the filaments [44]. $F_{if}$ was modeled by approximating the IFs as cylinders of radius r with uniform electron density ρ, described by the equation:

$$F_{if} = 2\pi\rho r^2 \frac{J_1(qr)}{qr} \quad (2)$$

where $J_1$ is a Bessel function of the first kind. $F_{mat}$ was assumed to be proportional to 1/q, reflecting scattering from random polypeptide coils filling the interfilamentous matrix. The intense background at low q values, $I_{BG} = B_2 + B_1 q^{-n}$, has been attributed by Briki et al. [44] to scattering from other components of the wool tissue, such as inter-macrofibrillar zones, the cuticle, *etc.* For the structure factor, the following equation was used [46], based on a hexagonal paracrystal model [45,47]:

$$Z(q) \propto \int_0^{\pi/2} \frac{1-F_1^2}{1-2F_1\cos(-qd_1\cos\varphi)+F_1^2} \frac{1-F_2^2}{1-2F_2\cos(qd_2\sin\varphi)+F_2^2} d\varphi \quad (3)$$

where:

$$F_1(q) = e^{-\frac{1}{2}\Delta^2 d_1^2 q^2} \text{ and } F_2(q) = e^{-\frac{1}{2}\Delta^2 d_2^2 q^2} \quad (4)$$

Here, $d_1$ and $d_2$ are the characteristic distances between the IFs [see Fig. 3(b)], and Δ (where $0 < \Delta < 1$) denotes the relative magnitude of lattice fluctuations along the two directions. The simulation provided the following values: 2r = 8.8 nm, a = 9.8 nm and Δ = 0.25. Small values

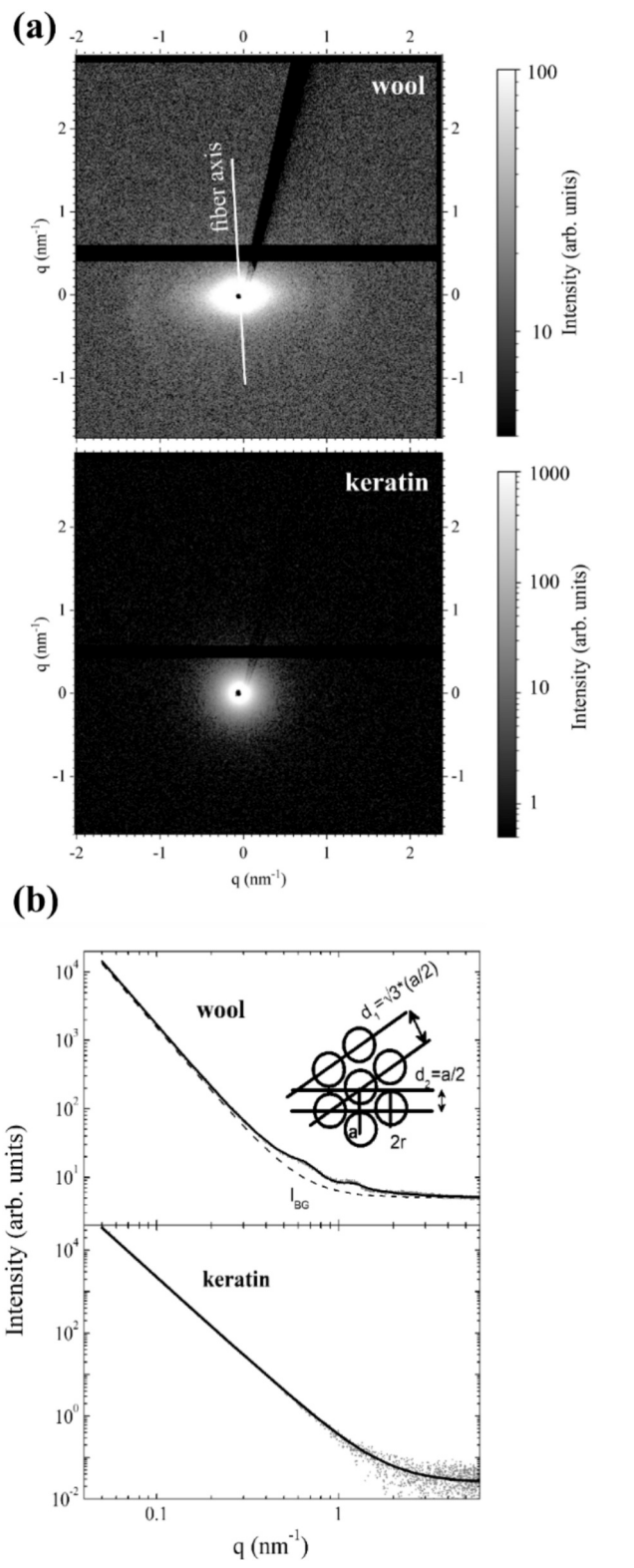


**Fig. 3. (a)** 2D SAXS scattering patterns of the wool fiber and the keratin powder, **(b)** Intensity *vs.* q curves for the wool fiber (equatorial integration) and keratin (pie integration) plotted as grey dots. The thick black lines represent the simulated curves, and the dashed line corresponds to the background contribution ($I_{BG}$). The parameter a denotes the lattice constant of the 2D hexagonal lattice of keratin IFs.

of Δ indicate a well-ordered 2D lattice. For the $I_{BG}$ background, n was found equal to 3.1. In contrast, for the keratin powder, no evidence of interference due to IF packing was observed. The scattering intensity could be described solely by the $I_{BG}$ contribution with $n = 3.9$. Therefore, the SAXS analysis revealed that the packing of IFs in the keratin sample was not preserved, or it is highly distorted after the extraction procedure from the wool.

### 3.2. Raman spectroscopy at ambient conditions

The Raman spectrum of α-keratin extracted from wool, measured at ambient conditions, is shown in Fig. 4. Background subtraction for the spectra recorded over a broad range (300–3600 cm$^{-1}$) was performed using a peak clipping algorithm [48], described in detail in the Supplementary Material (S2). The spectral region from 500 to 1800 cm$^{-1}$, known as the fingerprint region, contains vibrational modes characteristic of the molecular structure [49,50]. The peak at ~515 cm$^{-1}$ is attributed to S—S stretching vibrations in disulfide bridges formed within and between IFs [30]. The peaks at ~622 and ~ 644 cm$^{-1}$ are associated with C—C twisting modes of Phenylalanine (Phe) and Tyr, respectively [51,52]. Contribution in the latter due to C—S stretching from Cysteine (Cys) residues is not excluded [53]. Up to 1242 cm$^{-1}$, the spectrum contains a mixture of AA-specific bands [54] and α-helix backbone skeletal vibrations at ~935 cm$^{-1}$ [55]. The ring breathing of Phe gives rise to a sharp peak at 1003 cm$^{-1}$ [56,57]. The band centered at ~1450 cm$^{-1}$ corresponds to $CH_2$ and $CH_3$ deformation modes, primarily from side chains of various AAs [58]. The vibrational modes of the peptide bonds give rise to bands at ~1273 cm$^{-1}$ (amide-III) and ~ 1665 cm$^{-1}$ (amide-I) [55,58,59]. A shoulder peak at ~1613 cm$^{-1}$ is attributed to C—C ring stretching in aromatic AAs side chains [56,60]. The broad band at ~2934 cm$^{-1}$ arises from C—H stretching modes of side chains and the central C atom ($C_\alpha$-H) of AAs. When the carbon atom in the side chain belongs to an aromatic group, the peak shifts to ~3060 cm$^{-1}$ [61,62].

The Raman spectrum of keratin at 1 bar inside DAC after the pressure cycle up to approximately 4 GPa is also shown in Fig. 4. Comparison with the spectrum of keratin prior to DAC loading indicates that the pressure treatment did not induce any significant frequency shifts or changes in the lineshape of the characteristic Raman bands. The peak centered at 1332 cm$^{-1}$ and the broad band at 2140–2700 cm$^{-1}$ are attributed to first- and second- order Raman scattering of diamond (DAC), respectively [63–65]. The Raman spectrum of the fluorinert mixture used as PTM in the DAC is rather complex up to 1430 cm$^{-1}$, as depicted in Fig. 4, and strongly overlaps with the protein signal. Therefore, only the Raman spectrum of keratin at frequencies above 1400 cm$^{-1}$ could be meaningfully followed in our high-pressure measurements.

### 3.3. Raman spectroscopy under high pressure

The Raman spectra of α-keratin recorded under pressure are shown in Fig. 5. Three bands were followed upon pressure increase and decrease: 1400–1500, 1600–1700 and 2800–3100 cm$^{-1}$, arising from the $CH_2$ and $CH_3$ deformation modes of AA side chains, amide-I stretching vibration originating from 80 % ν(C═O) and 20 % ν(C—N) vibrations of the peptide bond [66], and C—H stretching predominately of the AA side chains, respectively. At low pressures, the bands are asymmetric, indicating that multiple components are required for accurate spectral fitting. However, upon pressure increase, the bands broadened, and some overlapping peaks had to be merged. The frequency positions of the peaks used for fitting at ambient conditions, along with their assignment, are included in Table 1.

The peak positions obtained from the fitting are plotted as a function of pressure in Fig. 6. Solid and open symbols represent measurements during pressure increase and decrease, respectively. Since pressure application causes peak broadening and apparent merging of some

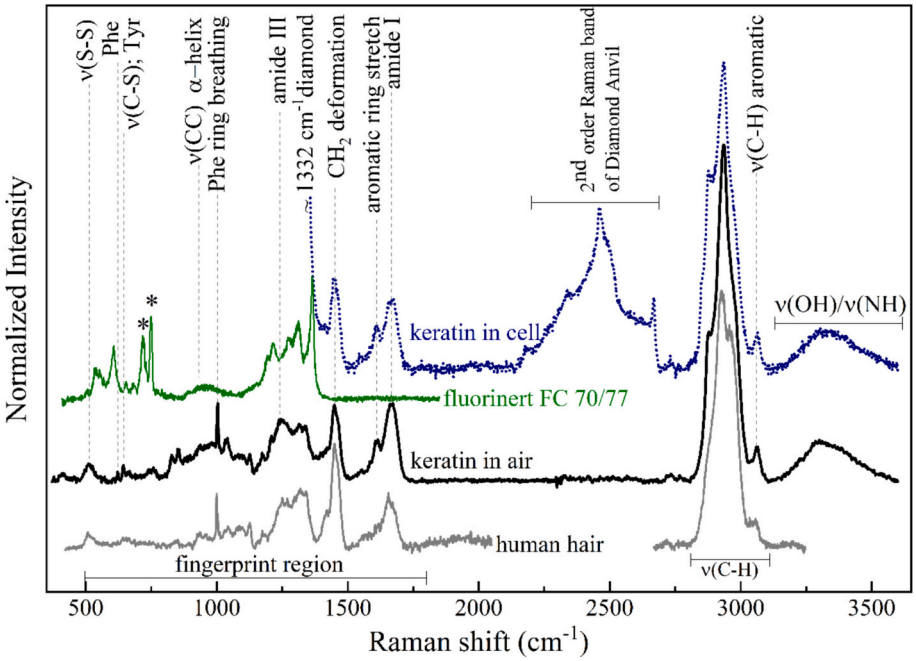


**Fig. 4.** Raman spectra of α-keratin at ambient conditions and inside the DAC at 1 bar after pressure release from ~4 GPa. Spectra of the PTM (fluorinert mixture) and human hair at ambient conditions are also included. The spectra are vertically shifted for clarity. Asterisks indicate the PTM peaks, which were monitored during pressure increase to confirm its hydrostatic behavior.

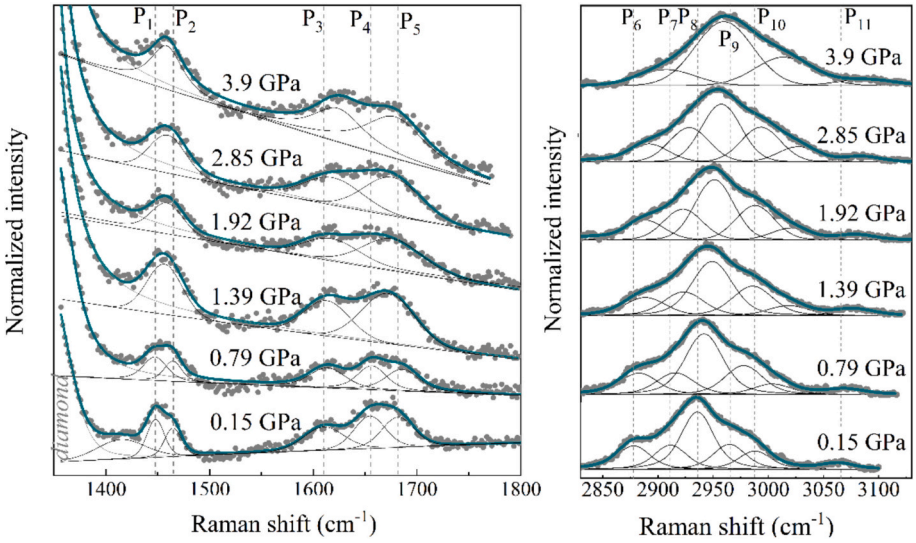


**Fig. 5.** Representative Raman spectra of keratin under pressure. Fitting of the (left) C—H deformation and amide-I bands, at *ca.* 1455 and 1670 $cm^{-1}$, respectively, and (right) the C—H stretching band centered at *ca.* 2935 $cm^{-1}$. Solid circles, thin, and thick lines correspond to the experimental data, the individual peaks used for the fitting, and the overall fitting curve, respectively. Vertical dotted lines mark the peak positions at ambient conditions.

peaks, the centroid of selected peak pairs is also plotted. At low pressures, these centroids, calculated as weighted averages of the contributing peak positions taking into consideration their integrated areas, follow the dependence observed at higher pressures in the case of C—H deformation and amide-I bands. Similarly, for the C—H stretching band shown in Fig. 6 (right), the grey circles represent the centroid of the $P_9$ and $P_{10}$ peaks. The pressure coefficients for each individual peak are listed in Table 1. Overall, the pressure-induced deformation of keratin appears to be reversible up to 4 GPa, as evidenced by the similar trends observed during pressure increase and decrease. It should be mentioned that the strongest Raman peaks of the PTM, marked with asterisks in Fig. 4, were also monitored across the pressure range. Their smooth response suggests a quasi-hydrostatic pressure behavior of the PTM.

In all cases, the Raman peak frequencies exhibited a linear increase with pressure. The least pressure-sensitive peak was the one corresponding to the deformation modes of C—H groups ($P_{1,2}$). Compared to their stretching modes (represented by $P_8$, the dominant peak in the C—H stretching band), they appear to be about four times less sensitive upon volume reduction. As far as the amide-I band is concerned, a positive pressure slope was found, reflecting its sensitivity to protein conformation and H-bonding. The α-helix secondary structure in keratin is stabilized by means of H-bonds (—N—H···O═C—) between the carbonyl oxygen of one AA and the amino group hydrogen of another one, typically four residues apart. In our data, the amide-I band required

**Table 1**
Assignment of the peaks used for the fitting of the keratin's Raman spectra [53–61], their frequencies at ambient pressure along with pressure coefficients. For comparison, the respective values for collagen using the same Fluorinert mixture as PTM are also included [40]. δ and $\nu$ denote deformation and stretching modes, respectively.

| Peak | Vibrational mode | Keratin | | Collagen[a] | |
|---|---|---|---|---|---|
| | | ω($cm^{-1}$) | $\partial\omega/\partial P$ ($cm^{-1}$/GPa) | ω($cm^{-1}$) | $\partial\omega/\partial P$ ($cm^{-1}$/GPa) |
| **P1** | $\delta(CH_2)$, $\delta(CH_3)$ in AA side chains | 1446 | 1.7 ± 0.3 | 1451 | 2.4 ± 0.8[b] |
| **P2** | | 1464 | | 1465 | 2.3 ± 0.3 |
| **P3** | $\nu(CC)_{aromatic}$ | 1612 | 2.2 ± 0.5 | – | – |
| **P4** | Amide-*I* (α-helix) | 1655 | 2.2 ± 0.4 | 1656 | −2.5 ± 0.6 |
| **P5** | Amide-*I* (β-sheet/β-turns) | 1680 | | 1675 | −1.2 ± 0.6 |
| **P6** | $\nu_s(CH_3)$ | 2878 | 7.0 ± 0.7 | 2882 | 10.8 ± 0.6 |
| **P7** | $\nu_{as}(CH_2)$ | 2911 | 6.2 ± 0.3 | – | – |
| **P8** | $\nu_{as}(CH_2)$/ $\nu(C_\alpha\text{-H})$ | 2936 | 6.5 ± 0.4 | 2938 | 6.6 ± 0.3 |
| **P9** | $\nu_{as}(CH_2)$ Glu/Gln[c] | 2965 | 9.4 ± 0.7 | – | – |
| **P10** | $\nu_{as}(CH_2)$ Asp/Asn[d] | 2988 | | 2986 | 5.5 ± 0.7 |
| **P11** | $\nu(CH)_{aromatic}$ | 3064 | 7.0 ± 0.7 | – | – |

[a] For the assignment of collagen's peaks, refer to [40].
[b] For $P > 2$ GPa and ~ 0 for $P < 2$ GPa [40].
[c] Glu; Glutamic Acid, Gln; Glutamine.
[d] sp; Aspartic Acid, Asn; Asparagine.

two components, $P_4$ and $P_5$, for accurate fitting. These peaks are attributed for α-helical and β-turn structures, with the latter appearing at higher frequencies due to weak or absent H-bonding [67]. According to Wang et al. [68], approximately one third of wool keratin adopts an α-helical structure with the remaining consisting of β-folded chains, β-angle and random conformations. In general, strengthening of the H-bond shifts the amide-I band to lower frequencies as it weakens the C═O bond [69]. H-bond strength increases with shorter H···O distances and/or as the bond angle between the —N—H and O═C groups approaches 180° (linear geometry). The positive slope found for the keratin amide-I band (2.2 ± 0.4 $cm^{-1}$/GPa) suggests that C═O bonds strengthen upon pressure application. This observation could be attributed to perturbation of the local geometry due to compression, resulting in misalignment and subsequent weakening of the H-bonds in the keratin chains. Although the pressure is applied isotropically, keratin exhibits anisotropic compression since the longitudinal and transverse moduli are different [70].

The high-pressure response of type-I collagen extracted from bovine Achilles tendon, has also been investigated using Raman spectroscopy [40]. The pressure slopes of various Raman peaks for collagen are compared with those of keratin in Table 1. Collagen, like keratin, is a structural fibrous protein of great significance, which is abundant in mammalians [71]. A key structural difference between the two proteins lies in their fundamental building units: keratin forms a coiled-coil structure, whereas collagen adopts a triple helix configuration [72]. Despite the fibrous character of both proteins, their responses to high pressure exhibit differences. The most notable one appears in the behavior of the amide-I band, which exhibits a negative pressure slope in collagen, opposite to what is observed in keratin. This observation can be attributed to the different structural role of H-bonds in stabilizing the respective structures (Fig. 7). In the α-helices of keratin dimers, H-bonds are formed between —C═O and H—N— of the same chain (intrachain) and parallel to the chain axis, stabilizing the helical conformation [Fig. 7 (a)]. In contrast, collagen features interchain H-bonding: the carbonyl oxygen (—C═O) of one chain forms a H-bond with the amide hydrogen (—N—H) of a neighboring chain with the bond axis oriented nearly perpendicular to the triple helix axis [Fig. 7(b)]. This network of interchain H-bonds is critical in stabilizing the triple helical structure. In collagen, the negative pressure slope of the amide-I band has been attributed to a shortening of the O···H distance upon pressure application, which in turn strengthens the interchain H-bonds [40].

Regarding the C—H modes, the main peak ($P_8$) of the keratin stretching band exhibits a pressure slope similar to that of collagen. This is notable given the distinct AA compositions of the two proteins (side columns in the heat map of Fig. 8). Despite these compositional differences, the hydrostatic pressure appears to induce comparable effects on the micro-environment around these groups. However, this similarity does not extend to the other peaks comprising the C—H stretching band. In keratin, peaks $P_6$ and $P_7$ exhibit pressure slopes similar to that of the main peak $P_8$, whereas $P_9$ and $P_{10}$ are more sensitive to pressure. In contrast, for collagen, $P_6$ shows a greater pressure sensitivity than $P_{10}$, highlighting differences in the molecular environment and mechanisms of volume adaptation. This suggests that even though the main C—H stretching mode behaves similarly upon pressure in both biomolecules, the additional components, linked to the AAs' side chain vibrations, respond differently due to distinct structural contexts. The frequencies of stretching modes (symmetric, $\nu_s$; asymmetric, $\nu_{as}$) associated with —$CH_3$, —$CH_2$ groups, and —C—H bonds in AAs' side chains and the $C_\alpha$—H in the peptide backbone, overlap significantly. Typically, they follow this ascending order [66]: $\nu_s(CH_2) < \nu_s(CH_3) < \nu_{as}(CH_2) < \nu_{as}(CH_3)$. The $C_\alpha$—H stretching mode frequency is moderately sensitive to the local chemical environment, including hydrogen bonding, secondary structure, and intermolecular interactions [75].

For a better interpretation of the differences in the pressure response of the C—H stretching bands of collagen and keratin, a comparison in their AA composition is essential. For that purpose, a heat map was constructed (Fig. 8), based on Raman spectra of individual proteinogenic AAs recorded at ambient conditions. As a first step, an XYZ matrix was generated, where Y corresponds to the AA, X to the Raman shift, and Z to the intensity of each spectrum, normalized by its total integrated area. The Raman spectra of keratin and collagen, recorded at ambient pressure, are shown on the top of the heat map. Additionally, Table S1 (Supplementary Material) provides the number of $CH_n$ ($n$ = 1,2,3) groups present in the side chain of each AA. It should be noted that the frequencies of the vibrational modes corresponding to the side chains of the AAs may shift upon incorporation into a macromolecular structure. Shifts of up to 10 $cm^{-1}$ have been reported [75].

Collagen's main AA constituents are Glycine (Gly), Proline (Pro)/

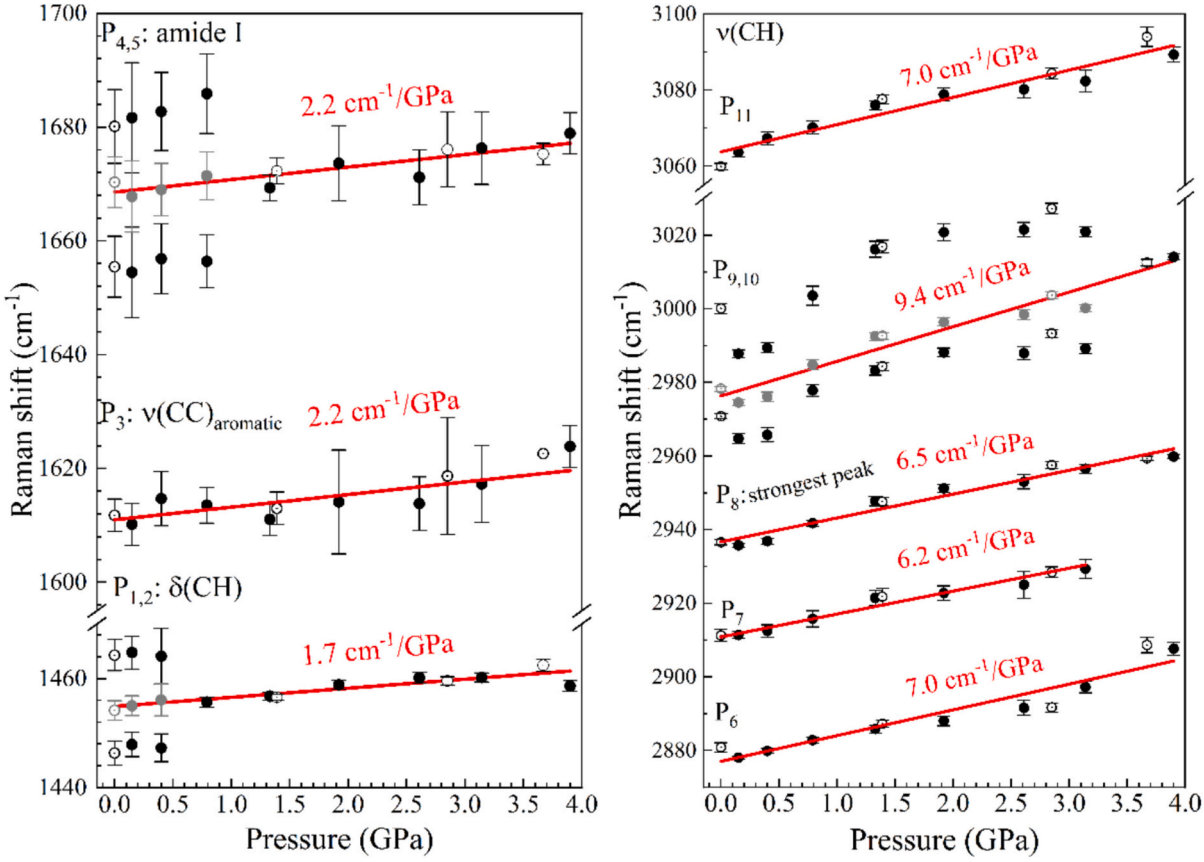


**Fig. 6.** Pressure dependence of the Raman peak positions: (left) $CH_2$ and $CH_3$ deformation, δ(CH), C—C stretching in aromatic rings, $\nu(CC)_{aromatic}$, and amide-I, (right) C—H stretching, ν(CH). Solid and open symbols correspond to pressure increase and decrease, respectively. Grey symbols indicate the centroid positions of two adjacent peaks that appear merged above a certain pressure value. Solid lines through the data represent their linear least-squares fits.

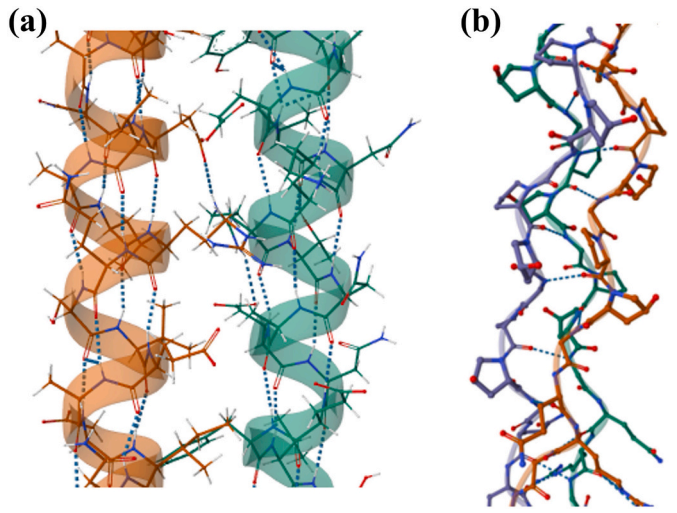


**Fig. 7.** (a) Molecular structure of α-keratin dimer. Hydrogen bonds, shown as thick dotted lines, are present in every pitch within one α-helix and are oriented almost parallel to the helix axis. (b) Molecular structure of type-I collagen. Hydrogen bonds, shown as thick dotted lines, are formed between different chains, contributing to the stabilization of the triple helix. Structures were obtained from Protein Data Bank (PBD IDs: 6EC0 and 7CWK) [73,74].

Hydroxyproline (Hyp) and Alanine (Ala) [71], which contribute to a prominent shoulder peak at ~2980 $cm^{-1}$ ($P_{10}$) in the Raman spectrum. Pro/Hyp are secondary amine AAs that contain a pyrrolidine ring imposing conformational rigidity. Due to steric constraints, Gly residues are positioned in the interior of the collagen triple helix, whereas Pro, Hyp and Ala are in the exterior. In contrast, keratin's major components include Glutamic acid/Glutamine (Glu/Gln) and Cysteine/Cystine (Cys/Cys-Cys), whose Raman bands appear at lower frequencies (Fig. 8). This difference likely explains the lower frequency maximum observed in the C—H stretching spectral region of the keratin spectrum compared to that of collagen. Furthermore, keratin's higher Tyr content results in a stronger contribution to its spectrum at 3050 $cm^{-1}$ and 1612 $cm^{-1}$. In the α-keratin coiled-coil, $CH_3$ groups are located predominantly in the interior of the dimer due to hydrophobic interactions [24,29]. A reasonable hypothesis arising from this arrangement is that the locally applied pressure on most $CH_3$ groups, with the exception of methyl group from threonine (Thr), is effectively reduced since these hydrophobic residues are buried in and between dimers. This may account for the lower pressure slope of $P_6$ (associated with methyl group vibrations) compared to $P_{9,10}$, which correspond to $\nu_{as}(CH_2)$ modes of AAs located in the methylene-rich exterior of the keratin dimers.

## 4. Conclusions

The response of α-keratin extracted from sheep wool under hydrostatic pressure was investigated using Raman spectroscopy. A non-polar pressure transmitting medium (Fluorinert mixture) was employed to avoid interactions with the protein. Overall, the compression up to 4 GPa was found to be a reversible process, indicating that no denaturation occurred within this pressure range. Furthermore, the absence of hysteresis in keratin's deformation upon pressure release confirms its elastic behavior at the molecular level. The Raman bands that could be monitored (*i.e.*, those not overlapping with the signal from the PTM or the DAC) showed a linear pressure dependence. Notably, the C—H

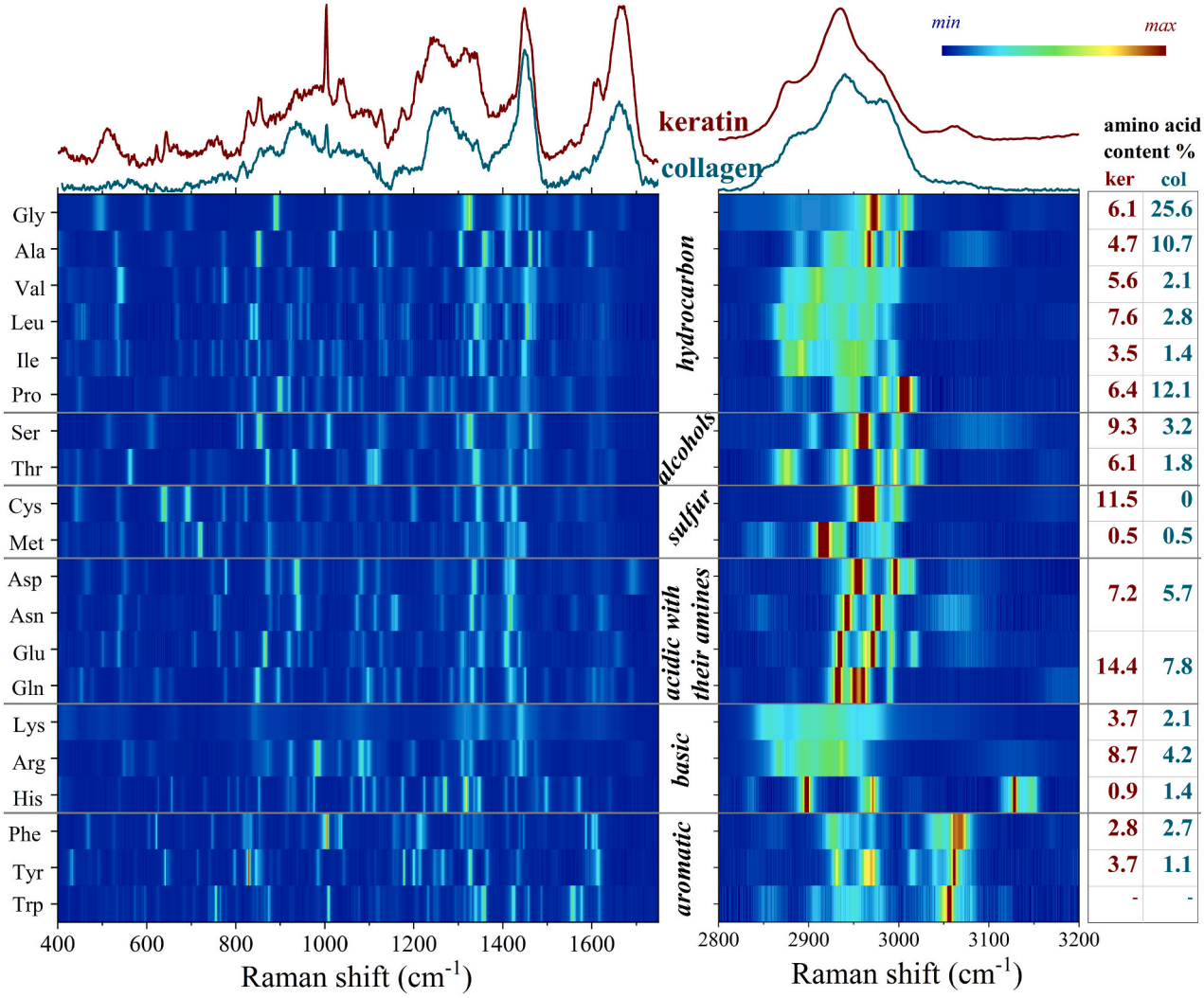


**Fig. 8.** Heat map of the proteinogenic AAs Raman signal. AAs are grouped based on the chemical nature of their side chains: hydrocarbon, alcohol, sulfur-containing, acidic (and their amines), basic and aromatic. The two columns on the right provide the representative composition of keratin [76] and collagen [77]. Raman spectra of Glycine (Gly), Valine (Val) and Lysine (Lys) were digitized from the Sigma-Aldrich reference database. The Raman spectra of keratin and collagen, recorded at ambient conditions, are shown on the top of the heat map for comparison. Note that the two spectral regions (left and right panels) are plotted using different intensity scales for clarity.

stretching vibrational modes were found to be almost four times more sensitive to compression than the C—H deformation modes. The positive pressure slopes observed for all studied Raman bands suggest a general stiffening of the C—H and peptide bonds (the amide-I is dominated by the C═O stretching vibration) upon compression. The amide-I frequency is highly sensitive to H-bonding. In α-helices, approximately one H-bond per AA residue is formed, oriented nearly parallel to the helix axis [2]. Upon hydrostatic compression, the C═O bond appears to strengthen, which implies a weakening of the H-bond, likely due to geometrical distortion that reduces the linearity of the O···H—N arrangement. This behavior contrasts with that of type-I collagen, where the amide-I band exhibits a negative pressure slope. In collagen, hydrogen bonds are formed primarily between adjacent chains in the triple helix, oriented perpendicularly to the helical axis. Compression in this case shortens the O···H distance, thereby strengthening the H-bonds. Finally, the different pressure slopes of the C—H stretching band components in keratin are attributed to variations in the local molecular environments. More specifically, most methyl groups reside within the hydrophobic interior of the coiled-coil keratin dimers, where they are shielded from direct compression. This spatial arrangement explains the lower pressure sensitivity of certain C—H modes compared to others located in the methylene-rich exterior.

## CRediT authorship contribution statement

**A.M. Paschou:** Writing – review & editing, Writing – original draft, Visualization, Validation, Investigation, Formal analysis, Data curation. **D. Christofilos:** Writing – review & editing, Supervision, Resources, Methodology, Investigation. **J. Arvanitidis:** Writing – review & editing, Supervision, Methodology, Investigation. **E. Pavlidou:** Resources, Investigation. **I. Zizak:** Resources, Investigation. **M. Katsikini:** Writing – review & editing, Writing – original draft, Supervision, Resources, Project administration, Methodology, Investigation, Funding acquisition, Conceptualization.

## Declaration of competing interest

The authors declare that they have no known competing financial interests or personal relationships that could have appeared to influence the work reported in this paper.

## Acknowledgements

The SAXS experiments at BESSY-II have been funded by the project NEPHEWS under Grant Agreement No 101131414 from the EU Framework Programme for Research and Innovation Horizon Europe. The authors also acknowledge the Center of Interdisciplinary Research and Innovation of the Aristotle University of Thessaloniki (CIRI−AUTH) for the access to the Raman instrumentation.

## Appendix A. Supplementary data

Supplementary data to this article can be found online at https://doi.org/10.1016/j.ijbiomac.2025.147401.

## Data availability

Data will be made available on request.

## References

[1] C.R. Chilakamarry, S. Mahmood, S.N.B.M. Saffe, M.A.B. Arifin, A. Gupta, M. Y. Sikkandar, S.S. Begum, B. Narasaiah, Extraction and application of keratin from natural resources: a review, 3 Biotech 11 (2021) 200, https://doi.org/10.1007/s13205-021-02734-7.

[2] B. Wang, W. Yang, J. McKittrick, M.A. Meyers, Keratin: Structure, mechanical properties, occurrence in biological organisms, and efforts at bioinspiration, Prog. Mater. Sci. 76 (2016) 229–318, https://doi.org/10.1016/j.pmatsci.2015.06.001.

[3] L. Ramms, G. Fabris, R. Windoffer, N. Schwarz, R. Springer, C. Zhou, J. Lazar, S. Stiefel, N. Hersch, U. Schnakenberg, T.M. Magin, R.E. Leube, R. Merkel, B. Hoffmann, Keratins as the main component for the mechanical integrity of keratinocytes, Proc. Natl. Acad. Sci. USA 110 (2013) 18513–18518, https://doi.org/10.1073/pnas.1313491110.

[4] B.S. Lazarus, C. Chadha, A. Velasco-Hogan, J.D.V. Barbosa, I. Jasiuk, M.A. Meyers, Engineering with keratin: a functional material and a source of bioinspiration, iScience 24 (2021) 102798, https://doi.org/10.1016/j.isci.2021.102798.

[5] D.A.D. Parry, A.C.T. North, Hard alpha-keratin intermediate filament chains: substructure of the N- and C-terminal domains and the predicted structure and function of the C-terminal domains of type I and type II chains, J. Struct. Biol. 122 (1998) 67, https://doi.org/10.1006/jsbi.1998.3967.

[6] D. Voet, J.G. Voet, C.W. Pratt, Biochemistry: Life at the Molecular Level, 3rd ed, John Wiley & Sons, New York, NY, 2008.

[7] L. Smeller, Biomolecules under pressure: phase diagrams, volume changes, and high pressure spectroscopic techniques, IJMS 23 (2022) 5761, https://doi.org/10.3390/ijms23105761.

[8] S. Shetty, S. Gokul, Keratinization and its disorders, Oman Med. J. 27 (2012) 348–357, https://doi.org/10.5001/omj.2012.90.

[9] P.G. Chu, L.M. Weiss, Keratin expression in human tissues and neoplasms, Histopathology 40 (2002) 403–439, https://doi.org/10.1046/j.1365-2559.2002.01387.x.

[10] J.C. Chamcheu, I.A. Siddiqui, D.N. Syed, V.M. Adhami, M. Liovic, H. Mukhtar, Keratin gene mutations in disorders of human skin and its appendages, Arch. Biochem. Biophys. 508 (2011) 123, https://doi.org/10.1016/j.abb.2010.12.019.

[11] J.-S. Li, Y. Li, X. Liu, J. Zhang, Y. Zhang, Strategy to introduce an hydroxyapatite–keratin nanocomposite into a fibrous membrane for bone tissue engineering, J. Mater. Chem. B 1 (2013) 432–437, https://doi.org/10.1039/C2TB00460G.

[12] A. Tachibana, Y. Nishikawa, M. Nishino, S. Kaneko, T. Tanabe, K. Yamauchi, Modified keratin sponge: binding of bone morphogenetic protein-2 and osteoblast differentiation, J. Biosci. Bioeng. 102 (2006) 425–429, https://doi.org/10.1263/jbb.102.425.

[13] T.R. Ham, R.T. Lee, S. Han, S. Haque, Y. Vodovotz, J. Gu, L.R. Burnett, S. Tomblyn, J.M. Saul, Tunable keratin hydrogels for controlled erosion and growth factor delivery, Biomacromolecules 17 (2016) 225–236, https://doi.org/10.1021/acs.biomac.5b01328.

[14] R. Nakata, A. Tachibana, T. Tanabe, Preparation of keratin hydrogel/hydroxyapatite composite and its evaluation as a controlled drug release carrier, Mater. Sci. Eng. C 41 (2014) 59–64, https://doi.org/10.1016/j.msec.2014.04.016.

[15] M. Borrelli, N. Joepen, S. Reichl, D. Finis, M. Schoppe, G. Geerling, S. Schrader, Keratin films for ocular surface reconstruction: evaluation of biocompatibility in an in-vivo model, Biomaterials 42 (2015) 112–120, https://doi.org/10.1016/j.biomaterials.2014.11.038.

[16] P.J. Apel, J.P. Garrett, P. Sierpinski, J. Ma, A. Atala, T.L. Smith, L.A. Koman, M. E. Van Dyke, Peripheral nerve regeneration using a keratin-based scaffold: long-term functional and histological outcomes in a mouse model, J. Hand. Surg. [Am.] 33 (2008) 1541–1547, https://doi.org/10.1016/j.jhsa.2008.05.034.

[17] Y.C. Lin, M. Ramadan, M. Van Dyke, L.E. Kokai, B.J. Philips, J.P. Rubin, K. G. Marra, Keratin gel filler for peripheral nerve repair in a rodent sciatic nerve injury model, Plast. Reconstr. Surg. 129 (2012) 67–78, https://doi.org/10.1097/prs.0b013e3182268ae0.

[18] S. Xu, L. Sang, Y. Zhang, X. Wang, X. Li, Biological evaluation of human hair keratin scaffolds for skin wound repair and regeneration, Mater. Sci. Eng. C Mater. Biol. Appl. 33 (2013) 648–655, https://doi.org/10.1016/j.msec.2012.10.011.

[19] D. Jao, Y. Xue, J. Medina, X. Hu, Protein-based drug-delivery materials, Materials 10 (2017) 517, https://doi.org/10.3390/ma10050517.

[20] A. Shavandi, T.H. Silva, A.A. Bekhit, A.E.-D.A. Bekhit, Keratin: dissolution, extraction and biomedical application, Biomater. Sci. (9) (2017) 1699–1735, https://doi.org/10.1039/C7BM00411G.

[21] R.K. Donato, A. Mija, Keratin associations with synthetic, biosynthetic and natural polymers: an extensive review, Polymers 12 (2020) 32, https://doi.org/10.3390/polym12010032.

[22] P.M. Steinert, A.C. Steven, D.R. Roop, The molecular biology of intermediate filaments, Cell 42 (1985) 411–419, https://doi.org/10.1016/0092-8674(85)90098-4.

[23] E. Fuchs, I. Hanukoglu, Unraveling the structure of the intermediate filaments, Cell 34 (1983) 332–334, https://doi.org/10.1016/0092-8674(83)90367-7.

[24] H.H. Bragulla, D.G. Homberger, Structure and functions of keratin proteins in simple, stratified, keratinized and cornified epithelia, J. Anat. 214 (2009) 516–559, https://doi.org/10.1111/j.1469-7580.2009.01066.x.

[25] R.S. Bear, H.J. Rugo, The results of X-Ray diffraction studies on keratin fibers, Ann. N. Y. Acad. Sci. 53 (1951) 627–648, https://doi.org/10.1111/j.1749-6632.1951.tb31964.x.

[26] D.A.D. Parry, P.M. Steinert, Intermediate filaments: molecular architecture, assembly, dynamics and polymorphism, Q. Rev. Biophys. 32 (1999) 99–187, https://doi.org/10.1017/S0033583500003516.].

[27] J.F. Conway, D.A.D. Parry, Structural features in the heptad substructure and longer range repeats of two-stranded α-fibrous proteins, Int. J. Biol. Macromol. 12 (1990) 328–334, https://doi.org/10.1016/0141-8130(90)90023-4.

[28] N. Geisler, J. Schunemann, K. Weber, Chemical cross-linking indicates a staggered and antiparallel protofilament of desmin intermediate filaments and characterizes one higher-level complex between protofilaments, Eur. J. Biochem. 206 (1992) 841–852, https://doi.org/10.1111/j.1432-1033.1992.tb16992.x.

[29] K.M. Bernot, C.H. Lee, P.A. Coulombe, A small surface hydrophobic stripe in the coiled-coil domain of type I keratins mediates tetramer stability, J. Cell Biol. 168 (2005) 965–974, https://doi.org/10.1083/jcb.200408116.

[30] D.A.D. Parry, Hard α-keratin intermediate filaments: an alternative interpretation of the low-angle equatorial X-ray diffraction pattern, and the axial disposition of putative disulphide bonds in the intra- and inter-protofilamentous networks, Int. J. Biol. Macromol. 19 (1996) 45–50, https://doi.org/10.1016/0141-8130(96)01099-9.

[31] E. Haimov, R. Windoffer, R.E. Leube, M. Urbakh, M.M. Kozlov, Model for bundling of keratin intermediate filaments, Biophys. J. 119 (2020) 65–74, https://doi.org/10.1016/j.bpj.2020.05.024.

[32] M. Essendoubi, M. Meunier, A. Scandolera, C. Gobinet, M. Manfait, C. Lambert, D. Auriol, R. Reynaud, O. Piot, Conformation changes in human hair keratin observed using confocal Raman spectroscopy after active ingredient application, Int. J. Cosmet. Sci. 41 (2019) 203–212, https://doi.org/10.1111/ics.12528.

[33] A. Kuzuhara, Analysis of structural change in keratin fibers resulting from chemical treatments using Raman spectroscopy, Biopolymers 77 (2005) 335–344, https://doi.org/10.1002/bip.20221.

[34] A. Kuzuhara, T. Hori, Analysis of heterogeneous reaction between reducing agents and keratin fibers using Raman spectroscopy and microspectrophotometry, J. Mol. Struct. 1037 (2013) 85–92, https://doi.org/10.1016/j.molstruc.2012.12.040.

[35] M. Essendoubi, N. Andre, B. Granger, C. Clave, M. Manfait, I. Thuillier, O. Piot, J. Ginestar, New approach for hair keratin characterization: Use of the confocal Raman spectroscopy to assess the effect of thermal stress on human hair fibre, Int. J. Cosmet. Sci. 44 (2022) 588–601, https://doi.org/10.1111/ics.12808.

[36] R. Paquin, P. Colomban, Nanomechanics of single keratin fibres: a raman study of the α-helix →β-sheet transition and the effect of water, J. Raman Spectrosc. 38 (2006) 504–514, https://doi.org/10.1002/jrs.1672.

[37] P. de T. Cavalcante Freire, J.A. Lima Jnior, B.T. de Oliveira Abagaro, G. de Sousa Pinheiro, J. de A. Freitas e Silva, J. Mendes, F.E. de Abreu Melo, High pressure raman spectra of amino acid crystals, Vib. Spectrosc. (2012), https://doi.org/10.5772/32533.

[38] N.A. Tumanov, E.V. Boldyreva, X-ray diffraction and Raman study of DL-alanine at high pressure: revision of phase transitions, Acta Crystallogr. B Struct. Sci. 68 (2012) 412–423, https://doi.org/10.1107/S0108768112028972.

[39] E.V. Boldyreva, High pressure studies of crystalline amino acids and simple peptides, in: Proceedings of the 4th International Conference on High Pressure Bioscience and Biotechnology 1, 2007, pp. 28–46, https://doi.org/10.11229/hpbb.1.28.

[40] A.M. Paschou, M. Katsikini, D. Christofilos, J. Arvanitidis, S. Ves, High pressure Raman study of type-I collagen, FEBS J. 285 (2018) 2641–2653, https://doi.org/10.1111/febs.14506.

[41] G. Benecke, W. Wagermaier, C. Li, M. Schwartzkopf, G. Flucke, R. Hoerth, I. Zizak, M. Burghammer, E. Metwalli, P. Müller-Buschbaum, M. Trebbin, S. Förster, O. Paris, S.V. Roth, P. Fratzl, A customizable software for fast reduction and analysis of large X-ray scattering data sets: applications of the newDPDAKpackage to small-angle X-ray scattering and grazing-incidence small-angle X-ray scattering, J. Appl. Crystallogr. 47 (2014) 1797–1803, https://doi.org/10.1107/s1600576714019773.

[42] A. Tiwari, I.S. Butler, J.A. Kozinski, A brief overview of the effect of high pressures on the vibrational spectra of biomaterials, Appl. Spectrosc. Rev. 44 (2009) 552–567, https://doi.org/10.1080/05704920903178421.

[43] H. Lee, K. Noh, S.C. Lee, I.-K. Kwon, D.-W. Han, I.-S. Lee, Y.-S. Hwang, Human hair keratin and its-based biomaterials for biomedical applications, Tissue Eng. Regen. Med. 11 (2014) 255–265, https://doi.org/10.1007/s13770-014-0029-4.
[44] F. Briki, B. Busson, J. Doucet, Organization of microfibrils in keratin fibers studied by X-ray scattering, Biochim. Biophys. Acta Protein Struct. Mol. Enzymol. 1429 (1998) 57–68, https://doi.org/10.1016/s0167-4838(98)00216-7.
[45] B. Busson, J. Doucet, Distribution and interference functions for two-dimensional hexagonal paracrystals, Acta Crystallogr. A 56 (2000) 68–72, https://doi.org/10.1107/s0108767399011174.
[46] K. Leppänen, S. Andersson, M. Torkkeli, M. Knaapila, N. Kotelnikova, R. Serimaa, Structure of cellulose and microcrystalline cellulose from various wood species, cotton and flax studied by X-ray scattering, Cellulose 16 (2009) 999–1015, https://doi.org/10.1007/s10570-009-9298-9.
[47] W. Wilke, M. Bratrich, Investigation of the superstructure of polymers during deformation by synchrotron radiation, J. Appl. Crystallogr. 24 (5) (1991) 645–650, https://doi.org/10.1107/S0021889890013243.
[48] C.G. Ryan, E. Clayton, W.L. Griffin, S.H. Sie, D.R. Cousens, SNIP, a statistics-sensitive background treatment for the quantitative analysis of PIXE spectra in geoscience applications, Nucl. Instrum. Meth. B 34 (1988) 396–402, https://doi.org/10.1016/0168-583x(88)90063-8.
[49] M.S. Bergholt, A. Serio, M.B. Albro, Raman spectroscopy: guiding light for the extracellular matrix, Front. Bioeng. Biotechnol. 7 (2019) 491962, https://doi.org/10.3389/fbioe.2019.00303.
[50] A.H. Chau, J.T. Motz, J.A. Gardecki, S. Waxman M.D., B.E. Bouma, G.J. Tearney M. D., Fingerprint and high-wavenumber Raman spectroscopy in a human-swine coronary xenograft in vivo, J. Biomed. Opt. 13 (4) (2008) 040501, https://doi.org/10.1117/1.2960015.
[51] Z. Movasaghi, S. Rehman, I.U. Rehman, Raman spectroscopy of biological tissues, Appl. Spectrosc. Rev. 42 (2007) 493–541, https://doi.org/10.1080/05704920701551530.
[52] J.W. Chan, D.S. Taylor, T. Zwerdling, S.M. Lane, K. Ihara, T. Huser, Micro-Raman spectroscopy detects individual neoplastic and normal hematopoietic cells, Biophys. J. 90 (2006) 648, https://doi.org/10.1529/biophysj.105.066761.
[53] A.C. Williams, H.G.M. Edwards, B.W. Barry, Raman spectra of human keratotic biopolymers: skin, callus, hair and nail, J. Raman Spectrosc. 25 (1994) 95–98, https://doi.org/10.1002/jrs.1250250113.
[54] D. Lin-Vien, N.B. Colthup, W.G. Fateley, J.G. Grasselli, Infrared and Raman Characteristic Frequencies of Organic Molecules, Academic Press Inc., San Diego, USA, 1991.
[55] F. Parker, Applications of Infrared, Raman and Resonance Raman Spectroscopy, Plenum Press, New York, 1983, pp. 83–110.
[56] R.C. Lord, N.-T. Yu, Laser-excited raman spectroscopy of biomolecules I. Native lysozyme and its constituent amino acids, J. Mol. Biol. 50 (1970) 509–524, https://doi.org/10.1016/0022-2836(70)90208-1.
[57] R.C. Lord, N.-T. Yu, Laser-excited Raman spectroscopy of biomolecules II. Native ribonuclease and α-chymotrypsin, J. Mol. Biol. 51 (1970) 203–213, https://doi.org/10.1016/0022-2836(70)90137-3.
[58] M. Gniadecka, O. Faurskov Nielsen, D.H. Christensen, H.C. Wulf, Structure of water, proteins, and lipids in intact human skin, hair and nail, J. Invest. Dermatol. 110 (1998) 393–398, https://doi.org/10.1046/j.1523-1747.1998.00146.x.
[59] J.T. Pelton, L.R. McLean, Spectroscopic methods for analysis of protein secondary structure, Anal. Biochem. 277 (2000) 167–176, https://doi.org/10.1006/abio.1999.4320.
[60] B. Li, Y. Sun, J. Yao, H. Wu, Y. Shen, C. Zhi, J. Li, An environment-friendly chemical modification method for thiol groups on polypeptide macromolecules to improve the performance of regenerated keratin materials, Mater. Des. 217 (2022) 110611, https://doi.org/10.1016/j.matdes.2022.110611.
[61] H.G.M. Edwards, Spectra-structure correlations in Raman spectroscopy, in: Handbook of Vibrational Spectroscopy, John Wiley & Sons Ltd., 2006, https://doi.org/10.1002/0470027320.s4103.
[62] D. Lin-Vien, N.B. Colthup, W.G. Fateley, J.G. Grasselli, The Handbook of Infrared and Raman Characteristic Frequencies of Organic Molecules, Academic Press Inc., San Diego, USA, 1991.
[63] T.V. Kovalenko, S.A. Ivakhnenko, Properties of diamonds seed grown in the Magnesium–Carbon system, J. Superhard Mater. 35 (2013) 131–136, https://doi.org/10.3103/S1063457613030015.
[64] D. Schiferl, M. Nicol, J.M. Zaug, S.K. Sharma, T.F. Cooney, S.-Y. Wang, T. R. Anthony, J.F. Fleischer, The diamond C13/12C isotope Raman pressure sensor system for high-temperature/pressure diamond-anvil cells with reactive samples, J. Appl. Phys. 82 (1997) 3256–3265, https://doi.org/10.1063/1.366268.
[65] S.A. Solin, A.K. Ramdas, Raman spectrum of diamond, Phys. Rev. B 1 (1970) 1687–1698, https://doi.org/10.1103/PhysRevB.1.1687.
[66] G. Socrates, Infrared and Raman Characteristic Group Frequencies Tables and Charts, Wiley & Sons, Hoboken, NJ, 2001.
[67] A.P. Fellows, M.T.L. Casford, P.B. Davies, Spectral analysis and deconvolution of the amide I band of proteins presenting with high-frequency noise and baseline shifts, Appl. Spectrosc. 74 (2020) 597–615, https://doi.org/10.1177/0003702819898536.
[68] Y. Wang, T. Zhang, F. Wang, L. Zhang, Y. Peng, M. Zhang, F. Ran, Efficient extraction of wool keratin governed by simultaneous cation and anion effects: from secondary structure studies to high α-helix keratin content, ACS Sustain. Chem. Eng. 12 (2024) 6003–6012, https://doi.org/10.1021/acssuschemeng.4c01055.
[69] W. Kauzmann, in: C.B. Anfinsen, M.L. Anson, Kenneth Bailey, John T. Edsall (Eds.), Advances in Protein Chem 14, Academic Press Inc, 1959, pp. 1–63.
[70] X. Tao, R. Postle, A viscoelastic analysis of the keratin composite, Text. Res. J. 59 (1989) 123, https://doi.org/10.1177/004051758905900301.
[71] K. Gelse, E. Pöschl, T. Aigne, Collagens—structure, function, and biosynthesis, Adv. Drug Deliv. Rev. 55 (2013) 1531–1546, https://doi.org/10.1016/j.addr.2003.08.002.
[72] M.D. Shoulders, R.T. Raines, Collagen structure and stability, Annu. Rev. Biochem. 78 (2009) 929–958, https://doi.org/10.1146/annurev.biochem.77.032207.120833.
[73] S.A. Eldirany, I.B. Lomakin, C.G. Bunick, Crystal Structure of the Wild-type Heterocomplex Between Coil 1B Domains of Human Intermediate Filament Proteins Keratin 1 (KRT1) and Keratin 10 (KRT10). doi: 10.2210/pdb6EC0/pdb.
[74] Y. Zhu, X. Yang, F. Sun. Structure of a Triple-Helix Region of Human Collagen Type I. doi:10.2210/pdb7cwk/pdb.
[75] N.K. Howell, G. Arteaga, S. Nakai, E.C.Y. Li-Chan, Raman spectral analysis in the C−H stretching region of proteins and amino acids for investigation of hydrophobic interactions, J. Agric. Food Chem. 47 (1999) 924–933, https://doi.org/10.1021/jf981074l.
[76] S.G. Giteru, et al., Compr. Rev. Food Sci. Food Saf. 22 (2023) 643–687, https://doi.org/10.1111/1541-4337.13087.
[77] M. Gauza-Włodarczyk, L. Kubisz, D. Włodarczyk, Amino acid composition in determination of collagen origin and assessment of physical factors effects, Int. J. Biol. Macromol. 104 (2017) 987–991, https://doi.org/10.1016/j.ijbiomac.2017.07.013.